https://doi.org/10.15407/ufm.22.03.352

A.P. SHAPOVALOV [1,2,*], M.O. BELOGOLOVSKII [2,3,], O.O. BOLIASOVA [1,4], and O.A. KORDYUK [1,2]**

[1] Kyiv Academic University of the N.A.S. of Ukraine and M.E.S. of Ukraine, 36 Academician Vernadsky Blvd., UA-03142 Kyiv, Ukraine
[2] G.V. Kurdyumov Institute for Metal Physics of the N.A.S. of Ukraine, 36 Academician Vernadsky Blvd., UA-03142 Kyiv, Ukraine
[3] Vasyl' Stus Donetsk National University, 21 600-richchya Str., UA-21021 Vinnytsia, Ukraine
[4] Donetsk Institute for Physics and Engineering named after O.O. Galkin of the N.A.S. of Ukraine, 46 Nauky Ave., UA-03028 Kyiv, Ukraine

* shapovalovap@gmail.com, ** belogolovskii@ukr.net

BINARY MOLYBDENUM COMPOUNDS: PROMISING MATERIALS FOR NOVEL PHYSICS OF SUPERCONDUCTIVITY AND PRACTICAL APPLICATIONS

This review article summarizes recent progress in low-temperature properties of binary molybdenum-based alloys and intermetallic compounds, focusing mainly on superconductivity characteristics reflecting novel physics as well as possible applications. We present experimental data proving two-band/two-gap nature of some superconducting compounds. As argued, the binary Mo–Re alloys with rhenium predominance represent an ideal and rare test system where related compounds with different Re/Mo ratios can be either centrosymmetrical or noncentrosymmetrical, leading in the latter case to possible mixed superconducting pairing. It is demonstrated that two MoC phases, namely, α-MoC and γ-MoC phases, are topologically nontrivial in their bulk and surface band structures, while amorphous MoSi and MoGe superconductors are among highly-promising materials for different superconductivity applications. We conclude the review with a brief discussion of new ten-dencies in computer modelling of the structure and properties of binary com-

Citation: A.P. Shapovalov, M.O. Belogolovskii, O.O. Boliasova, and O.A. Kordyuk, Binary Molybdenum Compounds: Promising Materials for Novel Physics of Superconductivity and Practical Applications, *Progress in Physics of Metals*, **22**, No. 3: 352–381 (2021)

pounds, using as an example recently discovered stoichiometric $MoBi_2$ compound, and practical prospects for already known and studied molybdenum-based superconductors.

Keywords: molybdenum-based compounds, superconductivity properties, two-band/two-gap materials, topologically nontrivial phases, superconductivity applications.

1. Introduction

Molybdenum is a shiny, silvery metal with medium density and moderate hardness (5.5 Mohs). It has the sixth highest melting point of all elements at 2623 °C. Among all engineering materials, it has the lowest thermal expansion coefficient and a rather high thermal conductivity. Stainless steel is the main application of molybdenum in modern industry. Molybdenum in steel is an alloying element that provides a significant increase in corrosion resistance. This property is mainly employed in building industry. In more severe conditions, where chlorinated seawater is a corrosive agent, grades with 6 or even 28 percentage of molybdenum are applied in steels or nickel-base superalloys, respectively. In the chemical industry, most of the molybdenum is used in the manufacture of catalysts and lubricants. Molybdenum catalysts belong to the group of heterogeneous catalysts, which together account for 80 percentage of the global catalyst market. Totally, these employments account for circa 90 percentage of the total use of molybdenum.

This review summarizes recent progress in low-temperature properties of binary Mo-based alloys and intermetallic compounds, focusing mainly on the superconductivity characteristics reflecting novel physics as well as possible applications in superconductor electronics, whose prospects due to unique combinations of thermal and electrical conductivity, thermal expansion, high-temperature strength, and environmental stability are just opening up to researchers [1]. It should be noticed that semiconductor-manufacturing equipment has long relied on molybdenum for components that require chemical stability, strength at elevated temperatures, and compatibility with corrosive process media. In particular, ion sources employ Mo because it resists reaction with dopant gases and erosion by the plasma inside the chamber. In molecular beam epitaxy machines, molybdenum is used as shutters, substrate carriers, and other internal components of the vacuum chamber. Physical vapour deposition processes require a material with high rigidity and flatness to ensure accurate reproducibility of the etched structure. It has been found that molybdenum does meet these requirements [1].

This paper aims to provide an up-to-date compendium of the available results on (sometimes-unique) physical properties of superconducting Mo alloys, physics behind them, and promising applications in superconducting electronics. The latter field of electronics is based on

functional electronic circuits incorporating active (nonlinear) and passive (linear) elements that are superconducting below the critical temperature T_c. Such circuits may exhibit unique characteristics and performance not attainable by conventional semiconductor electronics. However, as was emphasized by A.I. Braginski in his recent overview [2], the necessity of cooling to and operating at cryogenic temperatures is the main penalty that severely limits practical employments and constrains the superconducting electronics to remain a niche technology. As a result, it will be used only in cases of the extreme advantage in some particular cases (for example, as ultra-sensitive detectors of small magnetic fields) or when operation at very low temperatures is necessary for quantum performance (quantum computing). As for niche applications, besides SQUIDs (superconducting quantum interference devices) and quantum computers, we can mention ultrafast routers for communication networks, analogue-to-digital converters working in the microwave field and ultrasensitive digital receivers, which have no counterparts in the semiconductor world. Concerning quantum information science and technology, the greatest attention in this regard is attracted by superconducting quantum bits (qubits), electronic circuits comprising lithographically defined Josephson junctions, inductors, capacitors, and interconnects. Due to their potential for lithographic scalability, compatibility with microwave control, and operability at nanosecond time scales, they have moved to a leading position among related solid-state realization of basic elements for a quantum computer. A progress in this field is evident due primarily to improvements in their design, fabrication, and, importantly, their constituent materials and interfaces.

If we talk about materials, then, according to Braginski's expression [2], Nb remains to be the superconductor material workhorse with $T_c \approx 9$ K and conventional spin-singlet *s*-wave superconductivity that is well suitable for circuit operations typically at 4.2 K—the temperature when liquid helium boils at normal atmospheric pressure. Other conventional superconductors with much lower T_c than Nb are widely applied in radiation and particle detectors and in qubits. Those with T_c higher than that of Nb have not yet found widespread use. More than three decades passed since the discovery of first high-temperature superconductors did not bring the desired success in building electronic devices based on them, because process control at the sub-10-nanometer scale is required to make high-quality Josephson junctions out of these materials.

Molybdenum is an unremarkable low-temperature superconductor with a critical temperature $T_c = 915$ mK in the bulk state and somehow above value of 999 ± 11 mK for Mo films with thickness of above 35–40 nm [3]. There are a few reports of the T_c enhancement in amorphous thin films of Mo deposited at liquid helium temperature [4, 5]. In Ref. [5], the authors reported disorder induced superconductor–insulator

transition in molybdenum nanocrystalline thin films deposited at room temperature using DC magnetron sputtering under varying argon pressure. The grain size was tuned using deposition pressure as the only control parameter. In addition to the transition into an insulating state, they observed enhancement in T_c that depended upon the grain size and disorder in the films. The transition temperature initially increased with decreasing grain size up to values slightly above 5 K and then decreased, possibly due to the lack of coherence between neighbouring grains, thereby exhibiting a dome-shaped T_c-versus-deposition pressure phase diagram [5]. Notice that increasing disorder by reducing particle size is known to increase or decrease T_c depending on the coupling strength and the density of states at the Fermi level for a certain superconductor. Weakly coupled type-I superconductors as Al, Sn, In or Re in the disordered state demonstrate an increase in their T_c while type-II superconductor with intermediate or strong coupling like Nb and Pb reveal decreased superconducting gaps and T_c with reduction in particle size, see related references in Ref. [5]. The strong effect in molybdenum suggests that alloying is able to stabilize the relatively high-T_c phase and therefore to create novel superconducting materials useful for basic and applied research.

The main content of the review is divided into sections according to different alloying elements, rhenium, germanium, carbon, and silicon. The goal of each section is to highlight the exciting advances and future opportunities in the context of superconducting materials research. We also survey the most important concepts of related theoretical formalism in order to familiarize the reader with the necessary background for interpreting nontrivial spectroscopic findings in the Mo-based systems. In the second section, we discuss Mo–Re alloys, the most studied materials among binary alloys exhibiting two-gap behaviour, and explain, why two-band/two-gap superconductors are of particular interest in fundamental and practical terms (to complete the picture, in the third section, we provide evidences of two-band superconductivity in the ternary molybdenum–boron–phosphorus Mo_5PB_2 compound). In the second section, we also argue that the binary Mo–Re alloys with rhenium predominance represent an ideal and rare test system where related compounds with different Re/Mo ratios can be either centrosymmetrical or noncentrosymmetrical, leading in the latter case to possible mixed pairing. The fourth chapter turns attention to two examples from a rich MoC phase space, namely, α-MoC and γ-MoC phases, which are topologically nontrivial in their bulk and surface band structures. The fifth section deals with amorphous MoSi and MoGe superconductors, which are among highly promising materials for different superconductor applications. We conclude the review with a brief discussion of new tendencies in computer modelling of the structure and properties of binary

compounds, using as an example newly discovered stoichiometric $MoBi_2$ compound, and perspectives for already known and studied Mo-based superconductors.

2. Molybdenum–Rhenium Alloys

2.1. Basic Properties

Binary $Mo_{1-x}Re_x$ alloys are known to cover the full range of solid solutions and exhibit a rich phase diagram. While pure molybdenum and rhenium form body-centred-cubic (b.c.c.) and hexagonal close-packed (h.c.p.) structures, respectively, two other solid phases appear at intermediate Re/Mo ratios, namely, a tetragonal β-CrFe phase and a cubic α-Mn one [6]. It is interesting that the latter phase is a noncentrosymmetrical crystal structure that can be stabilized by annealing the sample over one week at 1400 °C in argon or hydrogen atmosphere. Mechanical and normal-state resistive properties of the compounds depend on which element is dominant. Mo-rich alloys are rather malleable while Re-rich compounds turned out to be extremely hard, and their electrical resistivity is much smaller than on the Re-rich side, thus, demonstrating the better metallicity of the b.c.c.-W-type phase. These two examples show a close relationship between the crystal structure and the basic characteristics of the $Mo_{1-x}Re_x$ alloys.

The authors of Ref. [7] measured electronic band dispersions for $Mo_{1-x}Re_x$ samples with $x \in [0; 0.25]$, applying angle-resolved photoemission spectroscopy, and calculated electronic densities of states for such alloys. Computational simulations, using the first-principles Korringa–Kohn–Rostoker coherent-potential approximation method, revealed the following changes in the density of states caused by the addition of Re: an overall shifting down due to the presence of the extra electron of Re and gradual widening and rounding of the sharp structures. Experimental data [7] showed that the bulk and most surface electronic bands shift relative to the Fermi level systematically and approximately rigidly with Re concentration. This result means that the rigid band model, in which the band structure and the density of states for the solvent metal remain unchanged upon alloying with a solute metal, is applicable to the molybdenum–rhenium alloys discussed below.

The latter statement characterized the general effect of alloying on the electronic structure of the Mo–Re samples but not its details. One of such deviations often named Lifshitz topological transition is an electronic topological effect that takes place in this system. Their idea can be traced back to the work by Ilya Lifshitz who related a change in the topology of the Fermi surface $\varepsilon(\mathbf{p}) = \varepsilon_F$ of a pure metal subjected to elastic strains to anomalies in thermodynamic quantities of metals [8] (see also Refs. [9] and [10]). The effect is arising due to the continuous

variation of some parameter (*e.g.*, pressure or impurity concentration), due to which the difference $z = \varepsilon_F - \varepsilon_c$ (here, ε_c is the critical energy, at which the topology of the constant energy surface changes, ε_F is the Fermi energy) passes through zero continuously. This leads to a change in the Fermi-surface connectivity, for example, the appearance of a new cavity or the rupture of a connecting neck when an external parameter is varied. At the temperature $T = 0$ K, the grand thermodynamic potential Ω acquires an irregular correction $\delta\Omega = -\alpha|z|^{5/2}$, and that is why this effect is sometimes called the 2½-order phase transition [9], referring to the Ehrenfest's terminology. At $k_BT << \varepsilon_F$, related anomalies manifest themselves not only in the thermodynamic characteristics of metals, but also in superconducting characteristics, as was evidenced by Brandt *et al.* in the paper [11] just by analysing pressure induced changes in superconducting properties of Tl–Hg alloys.

In fact, topology and alloying are often closely intertwined in condensed matter physics. In both cases, one seeks to characterize not the details of a particular band structure or disorder configuration, but the basic physics of the phenomenon. Returning to the $Mo_{1-x}Re_x$ alloys, we are referring to detailed first-principles calculations of their bulk electronic structure by Skorodumova *et al.* [12] who predicted two Lifshitz topological transitions occurring near the middle of the *N*–*H*-line in the bulk Brillouin zone at 2 and 6% Re concentration. Comparison of Fermi surfaces for pure Mo and $Mo_{0.75}Re_{0.25}$ in Ref. [7] confirmed it by revealing the van Hove singularity at 5% rhenium concentration, *i.e.*, very close to the theoretical predictions [12]. Recent results of resonant photoemission spectroscopy experiments [13] proved the existence of two electronic topological transitions at critical Re concentrations of $x_{c1} = 0.05$ and $x_{c2} = 0.11$.

It is known that the addition of rhenium to molybdenum improve the ductility of the material. The stress required to produce a fixed amount of strain higher than 3% is minimal around $x = 0.07$ [14]. Smith *et al.* [15] found phonon softening along the *N*–*H*-direction of the Brillouin zone when Mo–Re alloys undergo the Lifshitz transition, and it is just the location where a pocket of the Fermi surface appears when more than 5 at.% of rhenium is added to molybdenum [7]. Electronic states of the small group of carriers are localized due to the random potential introduced in the system when the composition is changed [16]. This effect should be very small and its detection requires very sensitive techniques. The author of Ref. [16] revealed large oscillations in the pressure dependence of T_c and in certain temperature derivatives of the normal-state thermoelectric power and resistivity and argued that the localization of electrons filling the new states due to the topological changes of the Fermi surface causes the observed oscillations in related characteristics. The localized states against a background con-

tinuum give rise to Fano resonance in photoemission spectroscopy measurements, which were detected in the $Mo_{1-x}Re_x$ system for $x > x_{c1} = 0.05$ [13]. This observation was interpreted as the result of the electron-like states localization in the newly appeared Fermi pocket. Now let us discuss how the changes in the topology influence superconducting properties of the alloys.

2.2. Effect of the Topology Changes on Superconductivity

2.2.1. Superconducting Characteristics

All $Mo_{1-x}Re_x$ alloys are superconducting with critical temperatures T_c exhibiting three different regions. To date, the Mo-rich side of the system was studied by different techniques (see Refs. [7, 17] and references therein). Systematic study of the full range of polycrystalline $Mo_{1-x}Re_x$ solid solutions was done in Ref. [6]. It was found that T_c values vary nonmonotonically with Re concentration, with the maximum value of 13 K being achieved for $x = 0.4$ [6, 18] without a change in the crystal structure. According to Ref. [13], it is an evident manifestation of the link between the electronic topological transitions in the Mo–Re system and superconducting properties. To reveal possible effect of the electronic density of states $N(\varepsilon)$, the authors of Ref. [18] performed related calculations and obtained that the Fermi level of Mo and the low-x alloys lies around a valley in the density of states and there is a small peak just above the Fermi level E_F. When Re is alloyed with Mo, the fine features are smeared out due to disorder effects and the energy dependence of the electronic density of states shifts to negative (lower) energies as it should be in a rigid-band model due to charge transfer from Re to Mo. The variation of $N(\varepsilon_F)$ as a function of x is shown in Fig. 1 with marker lines showing $x_{c1} = 0.05$ and $x_{c2} = 0.11$ corresponding to two topological transitions expected for this system. We see that $N(\varepsilon_F)$ slightly decreases for $x = 0.025$ as compared to $x = 0$ and then grows sharply as x is increased up to $x = 0.10$. For $x > 0.10$, $N(\varepsilon_F)$ increases with x, but with a much slower rate compared to $x < 0.10$. At $x = 0.40$, $N(\varepsilon_F)$ drops again in contrast to the $T_c(x)$ dependence. It means that the electronic density of states is not the only factor governing the critical temperature behaviour.

The elemental molybdenum is a compensated metal with higher mobility of holes than that of electrons [19]. Rhenium has one extra electron in comparison with molybdenum and its addition increases the number of electrons leading to crossing a new band by the Fermi level. In Ref. [18], it was shown that the appearance of Re 5*d*-like states at the Fermi energy above x_{c2} creates scattering of electrons between them and the rest of the bands through the electron–phonon interaction. This phonon-assisted interband scattering [18] leads to the enhancement of

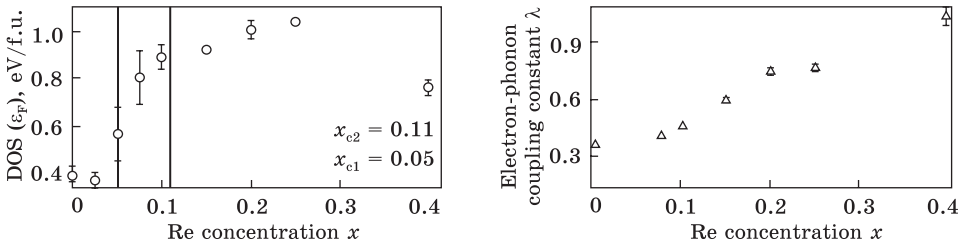

Fig. 1. Electronic density of states (DOS) at the Fermi level in $Mo_{1-x}Re_x$ as a function of x. Two vertical lines correspond to $x_{c1} = 0.05$ and $x_{c2} = 0.11$, which in one's turn correspond to two topological Lifshitz transitions. Adapted with permission from S. Sundar *et al.*, *New J. Phys.*, **17**: 053003 (2015). Copyrights 2015 Author(s), licensed under a Creative Commons Attribution 3.0 Licence [18]

Fig. 2. Electron–phonon coupling constant λ *vs.* the rhenium concentration x in $Mo_{1-x}Re_x$. Triangles represent λ values estimated from a strong-coupling relation for the heat-capacitance jump ΔC_S at $T = T_c$ and circles represent λ values found from the normal-state data combined with band-structure calculations. Adapted with permission from S. Sundar *et al.*, *New J. Phys.*, **17**: 053003 (2015). Copyrights 2015 Author(s), licensed under a Creative Commons Attribution 3.0 Licence [18]

the electron–phonon coupling constant $\lambda = 2\int_0^\infty \alpha^2 F(\omega)\omega^{-1}d\omega$, the dimensionless parameter characterizing the strength of the coupling of a specific electronic state to the whole phonon spectrum $F(\omega)$, $\alpha^2(\omega)F(\omega)$ is the Eliashberg spectral function [20]. As a result, first, the critical temperature T_c grows and, second, multiband superconductivity emerges [21, 22]. Using the heat capacitance $C(T)$ measurements, the authors of the paper [18] determined the jump ΔC_S at T_c and estimated $\lambda(x)$ dependence shown in Fig. 2. Let us stress again that enhanced T_c along with the two-gap superconductivity in the $Mo_{1-x}Re_x$ alloys are generated by the presence of the new Fermi pockets formed due to electronic topological transitions.

2.2.2. Lifshitz Transitions and Multiband Superconductivity

Now, we shall discuss why the two inherent features of the Mo–Re alloys, a topological Lifshitz transition and two-gap superconductivity, may considerably enhance the transition temperature to the superconducting state and possibly do it in the discussed compounds. From the superconductivity viewpoint, it is important that the proximity of the Fermi surface to van Hove singularities drastically enhances interaction effects and can lead to the emergence of a flat band, where all the states have the same energy [23]. Since the flat band has a huge density of electronic states, this may considerably increase the transition temperature T_c. G.E. Volovik [24] argued that this effect might be responsible for high-T_c superconductivity observed in pressurized hydrides just at

pressures when the system is close to the Lifshitz transition. Another origin of the enhanced T_c can be a Lifshitz transition between type-I Weyl and type-II Weyl points [25, 26]. Notice that, in ordinary superconductors, the singular density of electronic states emerging at the transition point generates nonanalytical behaviour of superconducting parameters as a function of the external factor modifying the shape of the Fermi surface [10, 27].

The presence of a second band in the electronic spectrum of a superconductor can have many other important consequences. In particular, an increased number of degrees of freedom in the condensate wave function may generate totally novel phenomena concerning the response to external perturbations that are lacking in single-gap superconductors. Such effects are that of relative phase and pair densities fluctuations in the distinct condensates predicted by Leggett [28] or the appearance of interband phase-difference solitons [29]. The presence of multiple bands qualitatively changes the nodal structure of a time-reversal-symmetry-breaking superconductor. Specifically, expected line or point nodes of an even-parity superconducting gap are replaced by two-dimensional Fermi surfaces of Bogoliubov quasi-particles, which are topologically protected [30]. Expectation of fundamentally new phenomena owing to multiband superconductivity stimulates the search for new materials clearly exhibiting the presence of, at least, two distinct gaps in the superconducting state.

The multiband nature of most functional materials, promising for practical applications, may not be reduced to a trivial increase in the number of adjustable parameters but is rather more fundamental. This fully applies to superconducting metals, for which a multiband modification of the Bardeen–Cooper–Schrieffer (BCS) theory was proposed in 1959 [31] but remained practically unclaimed until the discovery of superconductivity in magnesium diboride at the beginning of this century. In this material, two distinct groups of carriers with fundamentally different properties were discovered for the first time. The two energy gaps in the spectrum of elementary excitations below the critical temperature of the superconducting transition differ by almost three times [32].

The subsequent discovery of superconductivity in the iron-based superconductors [33] has contributed essentially to the conjecture that high-temperature superconductors are fundamentally multi-band and there is a certain correlation between T_c and proximity of the electronic structure of such metals to the topological transition of the Lifshitz's type [34–36]. Despite solid experimental evidence for such a correlation and certain efforts of theorists [10, 37], there is still no microscopic theory able to explain key mechanisms of this relationship and to provide specific recommendations for increasing T_c by controlled modification of the metal band structure.

At the same time, numerous experiments on magnesium diboride revealed lot of unconventional results such as a positive curvature of the upper critical field near T_c, a shoulder in the specific heat at intermediate temperatures, significant anisotropy of various characteristics, *etc.* Such unexpected behaviour does not necessarily mean two-band scenario but can also emerge from strong anisotropy in single-band materials, from non-*s*-wave gap symmetries, from a second superconducting phase, and other effects [38]. Therefore, the main goal of related experiments is to distinguish features arising from two-band effects from those of a completely different nature. Systematization and testing experiments for new samples, more simple than high-T_c superconductors, are vital for elucidating the impact of multiband effects on superconductivity. We believe that Mo–Re alloys can be one of them.

2.2.3. Heat Capacity and Superfluid Density of States in Mo–Re Alloys: Experimental Evidences for Two-Band Superconductivity

In the paper [21], the authors presented a detailed study of temperature and magnetic field dependences of the magnetization M and heat capacity C in $Mo_{1-x}Re_x$ alloys with $x = 0.25$ and 0.4, *i.e.*, above two topological transitions in the Fermi surface. Note that the $Mo_{0.6}Re_{0.4}$ alloy was identified as a strong coupling superconductor with the ratio of an energy gap $\Delta_0 = \Delta(T = 0\ \text{K})$ to T_c value $2\Delta_0/(k_B T_c) = 5.0$, which is well above the value of 3.52 predicted by the BCS theory of a weakly-coupled superconductor [39]. The normalized values of the heat-capacity jump at T_c, $\Delta C_S/(\gamma T_c)$ (γT is an electronic contribution to the normal-state heat capacity), are of about 1.7 and 2 for the $Mo_{0.75}Re_{0.25}$ and $Mo_{0.60}Re_{0.40}$ samples, respectively [21]. These values are substantially higher than the BCS value of 1.43 pointing out again that superconductivity in the binary $Mo_{1-x}Re_x$ alloys with $x > x_{c2}$ is at least nontrivial.

Figure 3 exhibits the temperature dependence of the ratio $\Delta C_S/(\gamma T_c)$ for the two Mo–Re compounds studied in Ref. [21]. The dotted lines in Figs. 3, *a* and *b* represent $C_S(T)$ behaviour in the superconducting state with a single isotropic superconducting gap $\Delta_0/k_B = 19.0 \pm 0.5$ K for the $Mo_{0.75}Re_{0.25}$ alloy and $\Delta_0/k_B = 26.5 \pm 0.6$ K for the $Mo_{0.60}Re_{0.40}$ alloy. We can see that experimental values of $C_S/(\gamma T_c)$ at low temperatures are systematically higher than calculated ones. Next, the authors fitted experimental data using an equation for a two-band superconductor

$$\frac{C_S(T)}{\gamma T_c} = \alpha \frac{C_{Ss}(T)}{\gamma_s T_c} + (1-\alpha)\frac{C_{Sl}(T)}{\gamma_l T_c}, \qquad (1)$$

with $C_{Ss}(T)$ and $C_{Sl}(T)$—contributions to heat capacity from the small (Δ_s) and the large (Δ_l) superconducting gaps, $\alpha = \gamma_s/(\gamma_s + \gamma_l)$ defines the fraction of the small gap, $\gamma_{s,l}$ are related normal-state coefficients. Now,

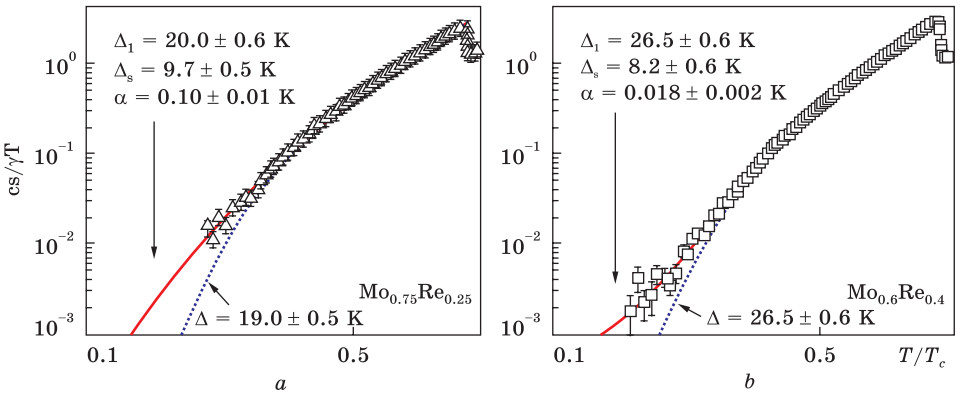

Fig. 3. Temperature-dependent electronic heat capacity in the superconducting state plotted vs. the T/T_c ratio for $Mo_{0.75}Re_{0.25}$ (*a*) and $Mo_{0.60}Re_{0.40}$ (*b*). Lines fit experimental data (open symbols) within single-gap (dotted lines) and two-gap (solid lines) theoretical approaches. Reprinted with permission from S. Sundar *et al.*, *J. Phys. Condens. Mater*, **27**, No. 4: 045701 (2015). Copyright 2021 IOP Publishing Ltd. [21]

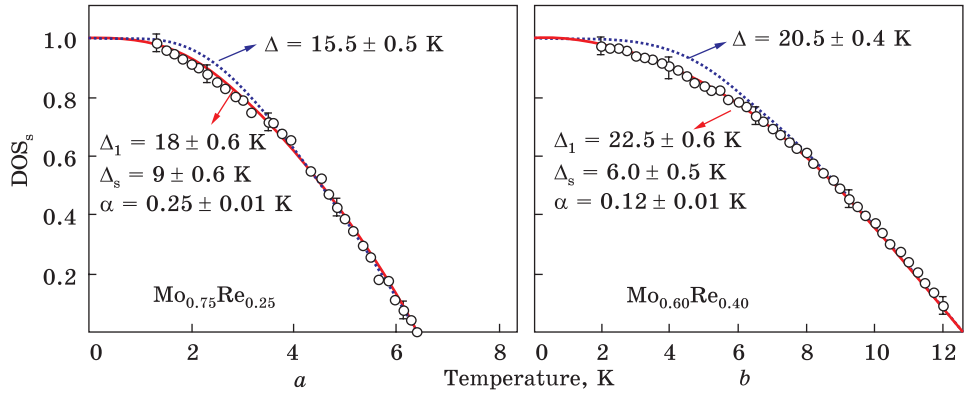

Fig. 4. Temperature-dependent superfluid DOS plotted as a temperature function for $Mo_{0.75}Re_{0.25}$ (*a*) and $Mo_{0.60}Re_{0.40}$ (*b*). Lines fit experimental data (open symbols) within single-gap (dotted lines) and two-gap (solid lines) theoretical approaches. Adapted with permission from S. Sundar *et al.*, *J. Phys. Condens. Mater*, **27**, No. 4: 045701 (2015). Copyright 2021 IOP Publishing Ltd. [21]

the resulting solid lines are perfectly consistent with the measured $C_S(T)$ data (see Fig. 3) where the values of Δ_s, Δ_1, and α are indicated. Notice that already in an earlier study of the temperature dependence of electronic heat capacity in $Mo_{0.60}Re_{0.40}$ alloy [39], a clear deviation from the single-gap behaviour was observed, while not analysed. It is evident that the existence of two superconducting gaps eliminates the discrepancy between theory and experiment.

Magnetization-*vs.*-magnetic field measurements at various temperatures made it possible to estimate the upper critical field $H_{c2}(T)$ depend-

ences as the field in the isothermal M–H-curves, at which the irreversible magnetization M giving rise to a hysteresis loop, reduces to zero. It was found that the temperature impact on H_{c2} estimated using the Werthamer–Helfand–Hohenberg model matches with the experimental curves only at temperatures close to T_c. The lower critical field H_{c1}, below which a type-II superconductor remains in the Meissner's state, was found analysing $dM(H)/dH$ dependences. For a superconductor in the local limit with $\xi(0) << \lambda$, $\xi(0)$ and λ are coherence length and penetration depth, the normalized superfluid density $\rho_S(T)$ reads as [21]

$$\rho_S(T) = \frac{\lambda^2(0)}{\lambda^2(T)} = \frac{H_{c1}(T)}{H_{c1}(0)}. \quad (2)$$

For a single-gap superconductor, $\rho_S(T)$ is given by [40]:

$$\rho_S(T) = 1 + 2\int_0^\infty N_S(\varepsilon, T)(df(\varepsilon, T)/d\varepsilon)d\varepsilon \quad (3)$$

with the Fermi–Dirac distribution function $f(\varepsilon)$ and the normalized density of single-particle states in a superconductor:

$$N_S(\varepsilon, T) = \mathrm{Re}\left(\frac{\varepsilon}{\sqrt{\varepsilon^2 - \Delta(T)^2}}\right). \quad (4)$$

Dotted lines in Figs. 4, *a*, *b* show the temperature dependence of normalized superfluid density calculated using Eq. (3) for an isotropic single-gap superconductor with $\Delta_0/k_B = 15.5 \pm 0.5$ K for the $Mo_{0.75}Re_{0.25}$ alloy and $\Delta_0/k_B = 20.5 \pm 0.4$ K for the $Mo_{0.60}Re_{0.40}$ alloy. Similar to Fig. 3, the estimated theoretical curve matches well with the experimental data at high temperatures while a marked deviation observed at low temperatures indicates possibility of the two-gap superconductivity. Acting like above (see Eq. (1)), the authors [21] got an excellent agreement between the two curves with parameters Δ_s, Δ_l, and α indicated in Fig. 4. These values noticeably differ from those in Fig. 3. Possibly, this is caused by the fact that the superfluid density estimated from H_{c1} is a local property whereas heat capacity is a bulk characteristic [21].

2.2.4. Junction Spectroscopy of Mo–Re Alloys: Experimental Evidences for Two-Band Superconductivity

In our opinion, the above arguments regarding a two-band/two-gap scenario in superconducting Mo–Re alloys (Figs. 3 and 4) only hint at their presence, while it would be desirable to obtain the related information from experiments that could give direct evidence of the two gaps without additional calculations. Tunnelling and point-contact spectroscopies are such techniques able to interpret the measured characteristics qualitatively without involving complex model concepts. The junctions used

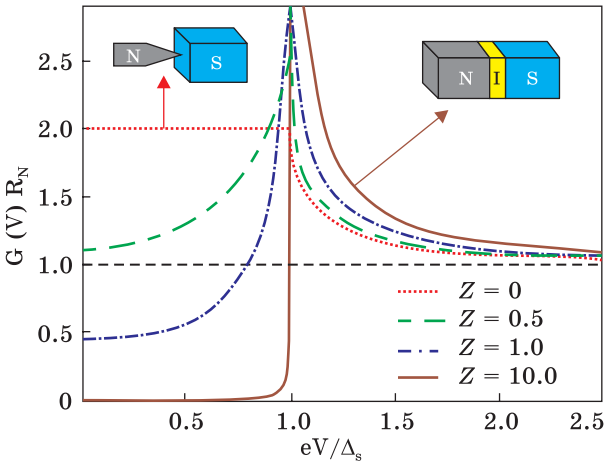

Fig. 5. Simulated differential conductance *vs*. voltage for zero-temperature coherent quantum transport across a one-dimensional *N*/*B*/*S*-trilayer with various barrier transparencies. Curves' shapes are controlled by the parameter *Z*. Two extreme limits, corresponding to a point contact ($Z = 0$) and a tunnel junction ($Z \gg 1$), are illustrated schematically. Reproroduced with permission from S. Volkov *et al.*, *Appl. Nanosci.*, 22 February (2021). Copyright 2021 Springer Nature [44]

for studying superconductors are usually formed by two metallic electrodes (at least, one of them is superconducting) divided by resistive, usually nanoscale region. Its task is to take over the entire voltage drop V applied to the setup creating thus a difference $\Delta\mu = \mu_L - \mu_R$ in chemical potentials of the left (L) and right (R) electrodes. Modifying the drop value, we are changing $\Delta\mu = eV$ and, thereby, probing energy spectra of unoccupied and occupied states in the excitation spectra of the junction electrodes.

Applying this idea, two extreme junction-spectroscopy techniques (tunnelling and point-contact) differ in the ways of creating the interlayer between two metals often called a weak link. A simplest version of the high-resistive interlayer is a narrow constriction between two wide electrically conducting regions, whose width is comparable to the electronic wavelength λ_F (see the inset in Fig. 5). The conductance G of such device known as a quantum point contact can be as small as $G_0 = 2e^2/h \approx 77.5$ μS—the universal conductance quantum [41]. This relation is valid for truly atomic dimensions when two bulk metals, reservoirs of electrons in local equilibrium, are connected by a quasi-one-dimensional single-atom constriction [42]. The G value grows with increasing the width w of the electron waveguide, through which a small integer number of transverse modes $N \approx 2w/\lambda_F$ can propagate at the Fermi level E_F. Tunnelling spectroscopy that played a central role in the experimental verification of the microscopic theory of superconductivity in traditional superconductors represents an opposite case of the interface transparency. Conventional tunnel junction shown schematically as an inset in Fig. 5 is planar with a several nm-thick oxide interlayer; an area prohibited by classical mechanics for electrons at the Fermi level of electrodes and, for this reason, often named a barrier (*B*). Hence, the difference between two main techniques is to a great extent quantitative, namely,

probabilities for charges to be transferred between junction electrodes in a certain quantum channel is near unity for the point-contact spectroscopy, while it is much less than unity in the tunnelling approach.

The most popular model to calculate the differential conductivity of the $N/B/S$-contact with a barrier of arbitrary transparency $G(V) = dI(V)/dV$, the derivative of the current I across the contact with respect to the voltage V applied to it, is that proposed by Blonder, Tinkham, and Klapwijk (BTK) [43]. The model assumes ballistic and one-dimensional character of the charge transport through a contact of N (normal) and S (superconducting) metals with a nanometer-thin scattering potential localized at the N/S-interface. Its effect is usually considered by introducing a potential barrier with a thickness d_B and the decay length l_B inside it. For a strong inequality $d_B << l_B$, transmission t and reflection r amplitudes read $t = i/(i - Z)$ and $r = Z/(i - Z)$, where i is the imaginary unit (see the details in the paper [44]).

Ultimately, the parameter Z determines the probability of electron transmission through the barrier $D = 1/(1 + Z^2)$ in the normal state as well as the reflection probability $R = 1 - D = Z^2/(1 + Z^2)$. The way of further calculations to find the ratio of differential conductance in superconducting $G_S(V)$ and normal G_N states is described in detail in the work [45]. Possible effect of inelastic-scattering processes in the superconductor is taken into account by introducing a constant imaginary part in the electronic energy $E \to E + i\Gamma$, where Γ is known as the Dynes parameter [46]. As a result, we have three adjustable parameters in a single-band superconductor, the energy gap Δ, the interface scattering efficiency Z, and the Dynes parameter Γ. In the case of a two-band superconductor, this number increases to seven: Δ_1, Δ_s, Z_1, Z_s, Γ_1, Γ_s and, finally, the weighting factor $w_1 < 1$ ($w_s = 1 - w_1$), which specifies the relative contribution of the two bands to the measured curve $G(V) = w_1G_1(V) + w_sG_s(V)$ [46].

In point contacts, the channels with the highest transmission probability determine the current along the device and, as a result, the scattering strength Z is nearly zero. In this case, for an electron (hole) incident on the interface from the N side at energies less than the superconducting energy gap Δ, the ballistic throughput across an $N/c/S$-point contact (c is the constriction) is dominated by a quantum process called Andreev reflection. Its details are as follow. An electron (hole), arriving from the N side, forms a Cooper pair in the S electrode reflecting back a hole (electron) of opposite spin and group velocity to the incident electron (hole) but with almost equal momentum. It is clear that this effect causes an enhancement of the conductance below the superconducting energy gap Δ, and the ratio of below-gap and above-gap conductance values equals 2 for an ideal point contact with a superconductor conventional in nature.

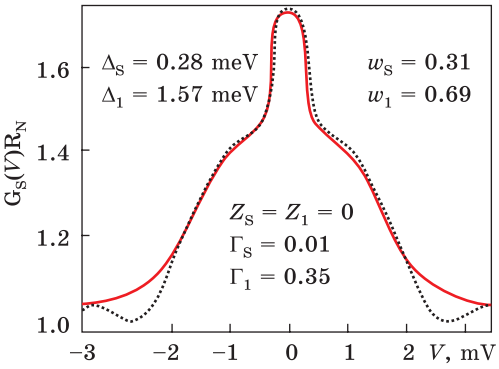

Fig. 6. Normalized differential conductance–versus–voltage curve measured for a representative point-contact sample formed by a silver tip and a $Mo_{0.52}Re_{0.48}$ alloy film (dots) compared with a fitting curve (solid line). The energy gaps differ markedly: Δ_s = 0.28 meV and Δ_l = 1.57 meV, the contribution of the band with a larger gap is dominant, the measurement temperature was 4.2 K

With increasing Z, the shape of the differential conductance $G(V)$ for an $N/I/S$-trilayer changes from a flat section at $|V| < \Delta/e$ to peaks at $|V| = \Delta/e$. From Fig. 5 illustrating these changes at very low temperatures, it is clear that the Andreev-reflection mechanism that defines the shape of the conductance spectrum for a point contact with $Z \approx 0$ as well as the tunnelling transport allow us to interpret measured $G(V)$ curves and to reveal the energy gap value qualitatively without involving complex model concepts.

We have performed two different kinds of the junction-spectroscopy experiments using Mo–Re-based point-contacts [47] and tunnelling trilayers [48]. In the first case, the N electrode was made of silver; its point contacts with the studied Mo–Re alloy were created both on film and bulk samples. Thin alloy layers with an approximately equal concentration of components, thicknesses ranging from 90 to 150 nm, and critical temperatures about 9 K were obtained by magnetron sputtering of a $Mo_{0.52}Re_{0.48}$ target. Structure and phase composition of the films were controlled by electron microscopy and electron diffraction, as well as by x-ray diffraction. The concentration of alloy components in the films determined using x-ray photoelectron spectroscopy with an accuracy of 5–6 at.% well corresponded to the target composition. Grain size spread was found to be tiny. This uniformity contributed to high resistance of the films to structural transformations and stable electrophysical properties during thermal cycling. The measured differential conductance spectra $dI(V)/dV$ of contacts based on Mo–Re alloys with approximately equal component contents revealed the presence of two energy gaps—larger Δ_l and smaller Δ_s ones. Typical $G(V)$ curve shown in Fig. 6 represents a sum of two similar characteristics of N/S-contacts with an almost ideal interface. The fitted parameters are indicated in the figure. Notice that, due to the small area of contacts, we got information only from individual microsize crystallites with different crystallographic directions, while, say, measurements of the electronic heat capacity for a molybdenum–rhenium alloy [21] provide characteristics

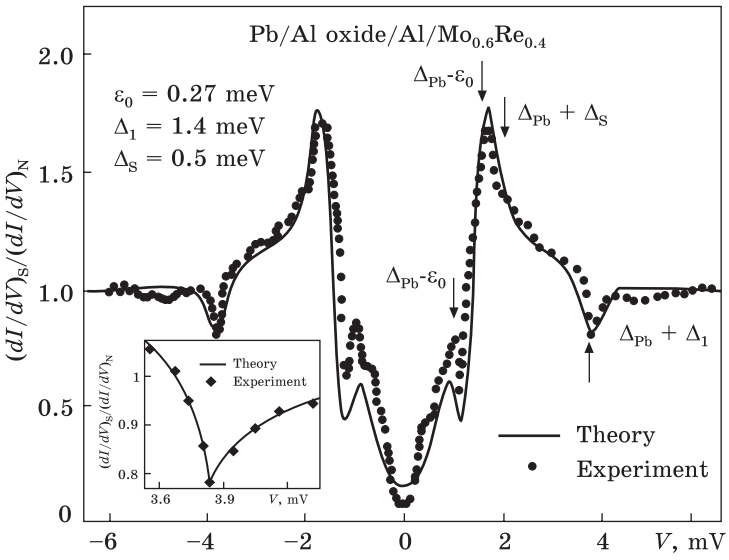

Fig. 7. Normalized differential conductance vs. voltage measured for a representative Pb/Al oxide/Al/$Mo_{0.60}Re_{0.40}$ tunnel junction (dotted curve) compared with a fitting curve (solid line). The arrows indicate gap-related features. The energy gaps Δ_s = 0.5 meV and Δ_1 = 2.5 meV reasonably agree with the values extracted from point-contact experiments (see Fig. 6), the contribution of the band with a smaller gap was dominant, the measurement temperature was 4.2 K. Reprinted with permission from V. Tarenkov *et al.*, *J. Supercond. Nov. Magn.*, **33**: 569 (2020). Copyright 2020 Springer Nature [48]

averaged over all directions. Local changes in superconducting properties in the near-surface region may be a source of the differences between surface-sensitive techniques and those dealing with the bulk.

In Ref. [48], we presented our results for tunnelling junctions based on $Mo_{0.60}Re_{0.40}$ polycrystalline films. The authors of Ref. [49] found that the native oxide of the Mo–Re alloy is grown up to thicknesses not more than 0.5 nm and are thinner that the oxides on Mo and Re surfaces. Therefore, in order to form a low-leakage tunnel junction on the Mo–Re film, they had to cover it with an Al overlayer oxidized after that. Following the work [49], we have used artificial Al-oxide tunnel barriers and a 100 nm-thick lead counter-electrode to form low-leakage tunnel junctions for measurements in the gap region not carefully analysed in previous tunnelling experiments [49]. If we are dealing with a two-gap superconducting electrode, $G(V)$ dependence for a tunnel junction should exhibit a two-peak structure. Figure 7 demonstrates representative conductance spectrum of the Pb/Al oxide/Al/$Mo_{0.60}Re_{0.40}$ junctions exhibiting reach fine structure with a prominent peak at 1.7 mV, a small local maximum on a steep slope at 1.0 mV, and a distinct dip at 3.8 mV

shown by related arrows. An analysis of the measured data based on a complex innergap structure in transport characteristics of superconducting junctions with degraded interfaces [50] permitted to extract the values of the energy gaps $\Delta_s = 0.5$ meV and $\Delta_l = 2.5$ meV. The presence of the two superconducting gaps in the Mo–Re alloy probed by tunnelling spectroscopy indicates that the more likely scenario of the T_c increase during alloying Mo with Re is interband interaction predicted in the seminal paper [31]. Notice that measurements of shot noise [50] and low-frequency $1/f$ noise [51] characteristics together with differential conductance spectra can provide more reliable information concerning the presence of two gaps in the superconductor studied [52].

2.3. Time-Reversal Symmetry Breaking in Mo–Re Alloys

Superconductors with a centrosymmetrical crystal structure can host spin-singlet- or spin-triplet states with even and odd parity, respectively. However, in noncentrosymmetrical superconductors, these strict symmetry-imposed requirements are relaxed, thus, implying the possibility of parity-mixed superconducting states. Because of it, such superconductors may display significantly different properties compared to their centrosymmetrical counterparts, *e.g.*, nodes in the superconducting gaps or broken time-reversal symmetry in the superconducting state. As was argued in Ref. [53], the rhenium-predominant binary Mo–Re alloys represent such an ideal and very rare test system where compounds with different Re/Mo ratios can be either centrosymmetrical or noncentrosymmetrical, while remaining superconducting. Muon-spin relaxation measurements, covering the whole Mo–Re phase diagram, showed that only $Mo_{1-x}Re_x$ alloys with $x = 0$ and 0.12 exhibit a broken time-reversal symmetry in their superconducting states. The latter statement includes also specific case of a $Mo_{0.23}Re_{0.77}$ alloy whose crystal structure can be both centrosymmetrical (h.c.p.-Mg phase) and noncentrosymmetrical (α-Mn) depending on the synthesis protocol. According to Ref. [53], it implies that the time-reversal symmetry breaking is not related to the noncentrosymmetrical crystal structure or to possible mixed pairing but, most likely, is due to the presence of rhenium.

The lack of inversion symmetry often induces antisymmetrical spin–orbit coupling, which splits the Fermi surface by lifting the degeneracy of the conduction-band electrons. If so, both inter- and intraband Cooper pairs with the same or with opposite spin directions can be formed. By increasing the strength of the antisymmetrical spin–orbit coupling, a fully gapped superconductor can be tuned into a nodal superconductor dominated by the spin-triplet pairing. Nevertheless, it is not the case of the Mo–Re system. Muon-spin relaxation [53] and zero-field specific-heat [6] results show that, despite a change in stoichiometry and differ-

ent crystal structures (both centro- and noncentrosymmetrical ones), alloys behave as fully gapped superconductors with dominant spin-singlet pairing. It was proven by comparing the temperature-dependent superfluid density behaviour extracted from the experiment with theoretical expectations in clean and dirty limits. In the first case, Eq. (3) was applied with the temperature dependence of the gap value following an approximate relation

$$\Delta(T) = \Delta_0 \tanh\left\{1.82\left[1.018\left(T_c/T - 1\right)\right]^{0.51}\right\} \quad (5)$$

taken from Ref. [54]. In the second case, when the coherence length ξ_0 is larger than the electronic mean-free path l_e, the temperature dependence of the superfluid density was assumed to be equal $\rho_S(T) = (\Delta(T)/\Delta_0) \tanh(\Delta(T)/(2k_BT))$. For $0.4 \le x \le 1$, ξ_0 and l_e have similar magnitudes and both formula for $\rho_S(T)$ describe very well low-T superfluid density in $Mo_{1-x}Re_x$ compounds and yield similar superconducting gap values [53].

In general, the study of β-CrFe- and b.c.c.-W-type superconducting phases with Re-dominating content [53] clearly imply that not only the Re presence, but also its amount is crucial for the appearance and the extent of time-reversal symmetry breaking in the Mo–Re superconductors.

3. Molybdenum–Boron–Phosphorus (Mo_5PB_2) Compound

3.1. Basic Properties

Mo_5PB_2 compound, which belongs to materials with a tetragonal Cr_5B_3-type structure, exhibits superconductivity with the highest critical temperature recorded in this family of compounds [55]. First-principle calculations indicate Mo_5PB_2 to be a multiband metal, whose density of states at the Fermi level is dominated by Mo 4*d*-orbitals and related zero-field heat-capacity measurement, suggest possible multigap features [55]. Temperature dependence of the electrical resistivity $\rho(T)$ measured from 300 to 2 K in zero magnetic field exhibits the metallic character. Magnetization experiments evidence the onset of superconductivity in Mo_5PB_2 at $T_c = 9.2$ K. Similar to Mo–Re alloys discussed above, muon-spin relaxation results allow to determine the temperature dependent inverse square of the magnetic penetration depth, which in turn is proportional to the superfluid density $\rho_S(T)$ (3). Careful analysis [56] based on the comparison of four possible models including single-gap *s*-, *p*-, and *d*-wave, and two-gap scenarios evidences fully gapped superconductivity in the Mo_5PB_2 compound. It is interesting that the two-gap approach to the interpretation of the $\rho_S(T)$ dependence provided almost identical results to the single-gap model. If to follow the two-gap scenario, then, the weight of the second gap is relatively small (0.25–0.3), and the derived gap values 1.11 and 1.57 meV are not significantly dif-

ferent that makes it difficult to discriminate between single- and two-gap superconductivity using only the temperature-dependent superfluid density. Therefore, more techniques had to be involved in the analysis.

3.2. Multigap Superconductivity

To reveal the multigap superconductivity in the Mo_5PB_2 compound, the authors of Refs. [55, 56] analysed the temperature effect on zero-field electronic specific heat in the superconducting state divided by the normal-state electronic specific heat $C_S(T)/(\gamma T)$ assuming a fully-gapped model. In Ref. [56], it was found that the single-gap model reproduces very well experimental data above $T = 0.4T_c$ with less satisfactory agreement below this value. At the same time, the two-gap approach shown in Fig. 8 by the solid line exhibits much better agreement across the full temperature range [56]. In agreement with the results of Ref. [55] ,this model gives two values $\Delta_s = 1.02$ meV, $\Delta_l = 1.49$ meV and $\alpha = 0.25$ (see Eq. (1)). We emphasize that the both gap values are greater than Δ_{BCS} expected in the weak-coupling regime, indicating strong-coupling superconductivity in Mo_5PB_2.

Further evidence for the two-gap superconductivity in the Mo_5PB_2 compound was brought in Ref. [56] by the field-dependent electronic specific heat coefficient $\gamma(H)$, the temperature-dependent upper critical field $H_{c2}(T)$, and electronic band-structure calculations. As follows from

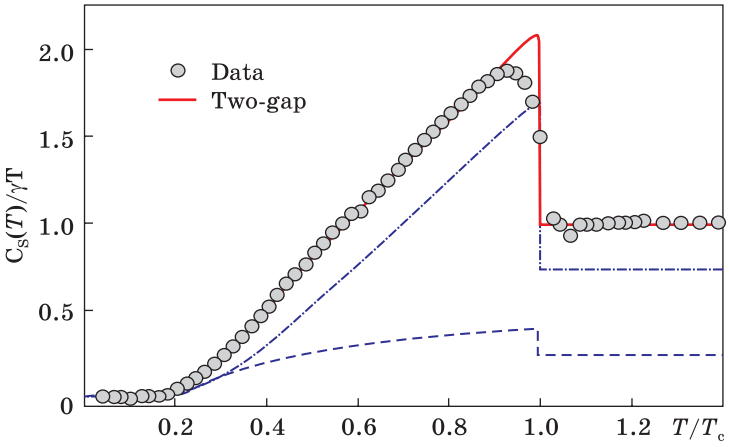

Fig. 8. The normalized electronic specific heat $C_S(T)/(\gamma T)$ of *vs*. the T/T_c ratio for Mo_5PB_2. Solid line represents the electronic specific heat calculated within a fully gapped *s*-wave model with two gaps. The dash–dotted and dashed lines represent individual contributions from the large and small superconducting gaps. Adapted with permission from T. Shang *et al.*, *New J. Phys.*, **22**: 093016 (2020). Copyright 2020 Author(s), licensed under the terms of the Creative Commons Attribution 4.0 Licence [56]

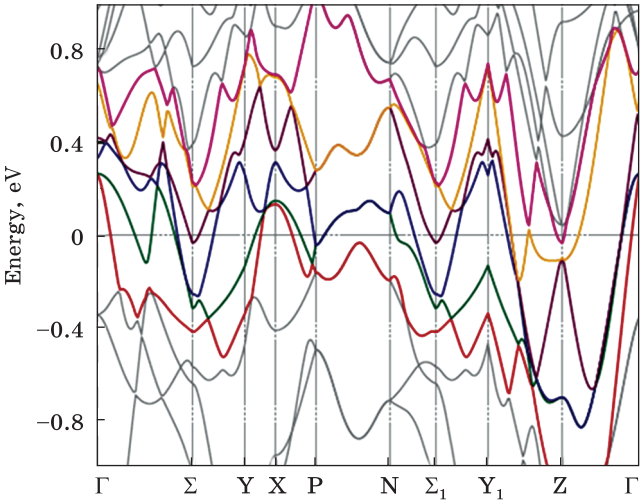

Fig. 9. Calculated electronic band structure of Mo_5PB_2. The various bands crossing the Fermi level are plotted in different colours (online). Reprinted with permission from T. Shang *et al.*, *New J. Phys.*, **22**: 093016 (2020). Copyright 2020 Author(s), licensed under the terms of the Creative Commons Attribution 4.0 Licence [56]

Fig. 9 and Table 1 in Ref. [56], six different bands are crossing the Fermi level, and the multiband features most probably originate from the different site symmetries of molybdenum atoms in the unit cell.

4. Molybdenum Carbide Compound

There are known three structural phases of molybdenum monocarbide, α-MoC, γ-MoC, and γ′-MoC. The superconductive α-phase of MoC forms in a rock-salt crystal structure with the lattice constant of 0.427 nm [57] and T_c of about 14 K [58]. The structure that was synthesized but with C deficiency is centrosymmetrical, both the Mo atom and the C atom in the unit cell can be regarded as space-inversion centres. The γ-phase of MoC, nonsuperconducting in its pristine form, has a noncentrosymmetrical hexagonal structure like tungsten monocarbide (WC) with lattice constants a = 0.290 nm and c = 0.281 nm [59]. The Mo layer is sandwiched between two C layers, and this trilayer structure forms a unit cell of γ-MoC. The γ′-MoC phase [59] is energetically not stable, and we will not discuss it later. All structures are found to be metallic without magnetism. The deposition process for the preparation of superconducting thin films of MoC by reactive magnetron sputtering in argon–acetylene atmosphere was described in Ref. [60]. Optimized deposition conditions permit to obtain smooth ultrathin MoC layers with the thicknesses from 5 to 20 nm. The critical temperature decreases with thinning the samples to 4.1 K for a 5 nm-thick MoC film [60]. The developed technology permitted to obtain strongly disordered 3 nm-thick MoC layers where the product of the Fermi wave number k_F and mean free path l, known as the Ioffe–Regel parameter, was close to unity [61].

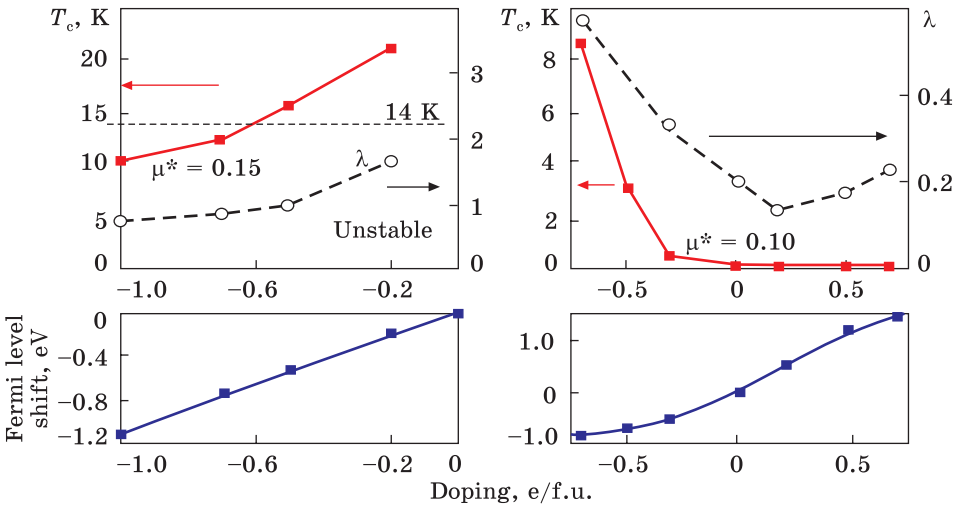

Fig. 10. Calculated superconducting transition temperatures and electron–phonon coupling strengths λ of α-MoC (left) and γ-MoC (right) phases. Transition temperatures T_c (solid lines) and electron–phonon coupling strengths λ (dashed lines) as functions of doping concentration (negative values correspond to hole doping). The lower part of the figure demonstrates Fermi-level shifts for corresponding dopings. Adapted with permission from A. Huang *et al.*, *Phys. Rev. Mater.*, **2**, No. 5: 054205 (2018). Copyright 2018 American Physical Society [62]

Using first-principles approaches, the authors of Ref. [62] studied electronic band spectra of α-MoC and γ-MoC compounds and found that both phases are topologically nontrivial in their bulk and surface band structures. They showed that α-MoC possesses a nonzero Z_2 topological invariant and Dirac surface states. On the other hand, γ-MoC is a topological nodal-line semimetal with drumhead surface states. Moreover, calculations performed within the virtual crystal approximation predict that the γ-phase of MoC gains superconductivity by hole doping and the critical temperature can be tuned even higher than 9 K. Therefore, both phases of MoC can be material candidates for studying the phenomenon of topological superconductivity.

To investigate the superconductivity and electron–phonon coupling properties in more details, the authors of Ref. [62] performed systematic simulations for the two phases of MoC using the density functional perturbation theory. They found that one of acoustic phonon bands of α-MoC becomes imaginary near the *X*-point. It means that α-MoC is unstable in its pristine form. The C deficiency effectively lowers the Fermi level, since the total number of electrons per formula unit decreases. This doping by holes removes the imaginary phonon modes and creates soft acoustic modes around *X*. At the same time, the lattice is stabilized in accordance with the experimental data. The soft phonon

modes couple strongly with electronic states and thus dominantly contribute to the effective electron–phonon coupling in the BCS theory.

Figure 10 demonstrates results of the calculations [62]. The transition temperature $T_c \cong 21.1$ K at doping level −0.2 electron per formula unit (e/f.u.) decreases gradually with the increasing concentration of the hole doping: $T_c \cong 15.7$ K for −0.5 e/f.u. hole doping similar to the experimental value of 14.3 K (Fig. 10, left). Therefore, the structural instability of α-MoC is responsible for the high superconducting transition temperature observed in this phase. As the hole doping concentration increases, soft phonon modes turn to normal ones, the effective electron–phonon interaction becomes weaker and, consequently T_c decreases. Unlike α-MoC, the crystal structure of γ-MoC is stable in its pristine form, but superconductivity was not observed in this phase. Calculations [62] showed that the transition temperature is negligibly small with or without electron doping. Doping by holes induces superconductivity in γ-MoC. T_c increases rapidly as the hole doping concentration grows and, for instance, $T_c = 8.6$ K at hole doping level of −0.7 e/f.u. (Fig. 10, right).

5. Amorphous Molybdenum Silicides and Germanides

Amorphous solids are disordered assembles of atoms or larger particles that nonetheless have a rigid structure. However, unlike crystalline solids, the rigidity of amorphous solids is not associated with a thermodynamically stable, stress-free microstructure. Starting from first studies of samples deposited on a cryogenically cooled substrate, amorphous superconducting materials have been the subject of numerous experimental and theoretical works [63]. Early work established that structural atomic disorder may promote an increase of the electron–phonon coupling upon going from the crystalline to the amorphous state. Some elements, which are poor superconductors in the crystalline phase (Ga and Bi) or even normal at all, as Be, become superconducting in the amorphous state. In many cases, the structural disorder enhances superconducting properties of nontransition pure metals, which are structurally stable only at very low temperatures [63]. On the contrary, amorphous alloys formed by transition metals are stable even during cycling between ambient and cryogenic temperatures [64–65]. Optimization of amorphous transition-metal films for specific superconducting applications is an actual problem of the metal physics.

MoSi and MoGe amorphous superconductors are among highly promising materials for different applications. Molybdenum silicide with a composition of $Mo_{0.75}Si_{0.25}$ has a bulk $T_c \approx 7.5$ K and the bulk superconducting energy gap $\Delta \approx 1.14$ meV, the critical current density at 1.7 K equals to 1.1–2.5 MA · cm^{-2} (see Table 1 in Ref. [66]). The molybdenum

germanide properties are very similar: the bulk $T_c \approx 7.4$ K, the bulk energy gap $\Delta \approx 1.1$ meV, the critical current density at 0.25 K equals to 1.2 MA · cm^{-2} (see Table 1 in Ref. [66] and Ref. [67]). Amorphous nature of both compounds allows for depositing them on a wide range of substrates without degradation of the superconducting material properties such as critical temperature and critical current density. Indeed, even for Mo–Si films as thin as 5 nm, $T_c = 5.5$ K [66], for Mo–Ge 7.5 nm-thick films, it equals to 4.4 K [67]. Therefore, the devices can operate using relatively cheap, less complex closed-cycle cryogenic systems [68].

Recent studies have identified the important role played by microstructure and short or medium-range order in amorphous materials in determining their physical properties, including superconducting characteristics [69]. By comparing T_c data with several theoretical models, the authors of Ref. [66] found that the room-temperature sheet resistance of Mo–Si films is strongly linked to the resulting T_c of the amorphous samples. Hence, an adequate description of structural disorder and its effect on the vibrational spectrum of amorphous metals is crucial for developing a consistent theory of phonon-mediated superconductivity in such materials. Related modification of the Eliashberg theory of strong-coupling phonon-mediated superconductivity was proposed in the recent paper [70]. According to the Anderson theorem, good crystalline superconductors are insensitive to nonmagnetic impurities and a sizable effect of disorder, which becomes apparent in the amorphous lattice structure, should be related to the excess of soft vibrational modes. It has been established that the largest part of the vibrational density of states of amorphous materials is made of 'diffusons'—excitations (neither plane wave like nor localized vibrational modes) propagating with a diffusive law due to intense scattering promoted by disorder [71]. The crossover from ballistic to diffusive transport is of the Ioffe–Regel type when the phonon wavelength becomes comparable to the mean free path [72]. As shown in Ref. [71], the low-frequency part of the Eliashberg function $\alpha^2F(\omega)$ is dominated by the two transverse modes, and this fact results in the nonmonotonic dependence of the electron–phonon coupling parameter $\lambda = 2\int_0^\infty \alpha^2F(\omega)\omega^{-1}d\omega$ introduced above on the diffusivity D of vibrational excitations. However, the excess of low-energy modes causes a decrease of the average phonon energy $\langle\omega\rangle$ upon going from crystalline to granular ordering (see Table 2 in Ref. [71] for respective values). If the latter factor is not too big to cancel the growth due to increased λ, then, an overall enhancement of T_c is possible. The interplay of the two factors can explain the difference between Pb-based materials, where introducing disorder leads to a decrease of the T_c even though λ increases monotonically in the amorphous state, and Al, where disorder results in T_c enhancement. The

previous conclusions relate only pure nontransition metals. We believe that molybdenum silicides and germanides can be an ideal test case for investigating disorder effects in transition-metal superconducting compounds.

6. Conclusions and Prospects

Extensive study of binary compounds has illuminated trends of elemental reactivity, quantified temperature- and composition-dependent phase stability, and led to the discovery of a huge number of new metallic materials. It was found that even small changes in chemical composition give rise to a wide variety of structures and physical properties [73]. This overview demonstrates that Mo-based binary alloys and intermetallic compounds are a versatile playground for exploring novel physical phenomena and, at the same time, have a strong potential for practical applications in superconducting electronics and spintronics. Unfortunately, diffuse, metallic bonding in such compounds presents a challenge for structure prediction and insight compared to ionically bonded systems, since, even in binary systems, the number of structures that has to be analysed is too large. Therefore, new strategies to address this problem are based on methods that combine modelling the electronic structure of known intermetallic materials with *ab initio* structure prediction algorithms that do not rely on known compounds for reference.

In the realization of novel metals with advanced physical parameters, the role of external factors modifying solid-state structures and, as a result, their properties is very important. In particular, the application of high pressures provides a tuneable parameter for promoting reactivity between elements that do not interact at ambient pressure even at high temperatures. As a result, the properties of the elements relative to each other are renormalized, leading to reactions that form novel materials, which appear exotic relative to ambient pressure phases (see Ref. [74] and references therein). The best example is the discovery of numerous new metallic hydrides exhibiting record-breaking superconducting critical temperatures [75].

Let us now refer to recent combined computational and experimental exploration of the Mo–Bi system, for which no binary intermetallic structures were previously known [74]. It has been established that the ambient pressure reactivity of Bi is limited, probably, due to the extreme chemical softness of this heavy element [76]. This behaviour changes significantly with the application of pressures, and the investigation of high-pressure transition metal–Bi phases reveals rich chemistry over a range of pressures. Using the density functional theory-based random structure searching approach, the authors of Ref. [74] explored a high-pressure phase space of the Mo–Bi system and predicted stability

of the stoichiometric compound $MoBi_2$ of the $CuAl_2$-structure type above 35 GPa. Related experiments performed in diamond anvil cells confirmed experimentally realization of the computationally predicted $CuAl_2$-type $MoBi_2$ structure at 35.8 GPa. This finding reveals a viable route toward controlling bonding and electronic properties through variation in the transition-metal element identity and indicates that the $CuAl_2$ structure is common in high-pressure Bi systems. The identification of two distorted $MoBi_2$ phases dynamically stable at ambient conditions *via* phonon dispersion calculations indicates that the proposed in Ref. [74] combined computational and experimental approach may be a promising means for directed synthesis of mixed metal systems with favourable properties.

This review presented a short overview of already known binary Mo-based compounds from the viewpoint of their superconducting characteristics. Of course, the range of their possible applications in other areas is much wider. Moreover, it cannot be ruled out that new binary Mo-based compounds with exceptional physical and chemical properties can be created using high pressures, similar to how it was done in the work [74] cited above. The further progress in this field requires joint coordinated efforts of experimenters and computational scientists.

Acknowledgements. This work was carried out within the framework of the Project 2020.02/0408 funded by the National Research Foundation of Ukraine and the Project No. 0120U102059 funded by the Fundamental Research Programme of the Ministry of Education and Science of Ukraine.

REFERENCES

1. *Applications of Molybdenum Metal and Its Alloys* (London: IMOA: 2013); https://www.imoa.info/download_files/molybdenum/Applications_Mo_Metal.pdf
2. A.I. Braginski, *J. Supercond. Nov. Magn.*, **32**: 23 (2019); https://doi.org/10.1007/s10948-018-4884-4
3. L. Fabrega, A.Camyn, P. Strichovanec, and C. Pobes, *IEEE Transactions on Applied Superconductivity*, **29**, No. 5: 2100405 (2019); https://doi.org/10.1109/TASC.2019.2903994
4. A. Hirakawa, K. Makise, T. Kawaguti, and B. Shinozaki, *J. Phys.: Cond. Mat.*, **20**, No. 48: 485206 (2008); https://doi.org/10.1088/0953-8984/20/48/485206
5. S. Sharma, E.P. Amaladass, N. Sharma, V. Harimohan, S. Amirthapandian, and A. Mani, *Physica B*, **514**: 89 (2017); https://doi.org/10.1016/j.physb.2017.03.044
6. T. Shang, D.J. Gawryluk, J.A.T. Verezhak, E. Pomjakushina, M. Shi, M. Medarde, J. Mesot, and T. Shiroka, *Phys. Rev. Materials*, **3**, No. 2: 024801 (2019); https://doi.org/10.1103/PhysRevMaterials.3.024801
7. M. Okada, E. Rotenberg, S.D. Kevan, J. Schafer, B. Ujfalussy, G.M. Stocks, B. Genatempo, E. Bruno, and E.W. Plummer, *New J. Phys.*, **15**: 093010 (2013); https://doi.org/10.1088/1367-2630/15/9/093010

8. I.M. Lifshitz, *Sov. Phys. JETP*, **11**, No. 5: 1130 (1960); http://www.jetp.ac.ru/cgi-bin/dn/e_011_05_1130.pdf
9. I.M. Lifshitz, M.Ya. Azbel, and M.I. Kaganov, *Electron Theory of Metals* (New York: Consultant Bureau: 1973).
10. Y.M. Blanter, M.I. Kaganov, A.V. Pantsulaya, and A.A. Varlamov, *Phys. Rep.*, **245**, No. 4: 159 (1994); https://doi.org/10.1016/0370-1573(94)90103-1
11. N.B. Brandt, N.I. Ginzburg, T.A. Ignat'eva, B.G. Lazarev, L.S. Lazareva, and V.I. Makarov, *J. Exp. Theor. Phys.*, **22**, No. 1: 61 (1966); http://www.jetp.ac.ru/cgi-bin/dn/e_022_01_0061.pdf
12. N.V. Skorodumova, S.I. Simak, I.A. Abrikosov, B. Johansson, and Yu.Kh. Vekilov, *Phys. Rev. B*, **57**, No. 23: 14673 (1998); https://doi.org/10.1103/PhysRevB.57.14673
13. L.S. Sharath Chandra, S. Sundar, S. Banik, S.K. Ramjan, M.K. Chattopadhyay, S.N. Jha, and S.B. Roy, *J. Appl. Phys.*, **127**, No. 16: 163906 (2020); https://doi.org/10.1063/1.5143836
14. D.L. Davidson and F.R. Brotzen, *Acta Metall.*, **18**, No. 5: 463 (1970); https://doi.org/10.1016/0001-6160(70)90132-X
15. H.G. Smith, N. Wakabayashi, and M. Mostoller, *Proceedings of Second Rochester Conference on Superconductivity in d- and f-band Metals* (Ed. D.H. Douglass) (New York: Plenum Press: 1976), p. 223.
16. T.A. Ignat'eva, *Phys. Solid State*, **49**: 403 (2007); https://doi.org/10.1134/S106378340703002X
17. T.A. Ignatyeva and A.N. Velikodny, *Low Temp. Phys.*, **30**: 388 (2004); https://doi.org/10.1063/1.1739133
18. S. Sundar, L.S. Sharath Chandra, M.K. Chattopadhyay, S.K. Pandey, D. Venkateshwarlu, R. Rawat, V. Ganesan, and S.B. Roy, *New J. Phys.*, **17**: 053003 (2015); https://doi.org/10.1088/1367-2630/17/5/053003
19. W.R. Cox, D.J. Hayes, and F.R. Brotzen, *Phys. Rev. B*, **7**, No. 8: 3580 (1973); https://doi.org/10.1103/PhysRevB.7.3580
20. E.L. Wolf, *Principles of Electron Tunneling Spectroscopy* (New York: Oxford University Press: 2012); https://doi.org/10.1093/acprof:oso/9780199589494.001.0001
21. S. Sundar, L.S. Sharath Chandra, M.K. Chattopadhyay, and S.B. Roy, *J. Phys. Condens. Mater*, **27**, No. 4: 045701 (2015); https://doi.org/10.1088/0953-8984/27/4/045701
22. S. Sundar, S. Banik, L.S. Sharath Chandra, M.K. Chattopadhyay, T. Ganguli, G.S. Lodha, S.K. Pandey, D.M. Phase, and S.B. Roy, *J. Phys. Condens. Mater*, **28**, No. 31: 315502 (2016); https://doi.org/10.1088/0953-8984/28/31/315502
23. D. Yudin, D. Hirschmeier, H. Hafermann, O. Eriksson, A.I. Lichtenstein, and M.I. Katsnelson, *Phys. Rev. Lett.*, **112**, No. 7: 070403 (2014). https://doi.org/10.1103/PhysRevLett.112.070403
24. G.E. Volovik, *Phys.-Usp.*, **61**, No. 1: 89 (2018); https://doi.org/10.3367/UFNe.2017.01.038218
25. D. Li, B. Rosenstein, B.Ya. Shapiro, and I. Shapiro, *Phys. Rev. B*, **95**, No. 9: 094513 (2017); https://doi.org/10.1103/PhysRevB.95.094513
26. M. Alidoust, K. Halterman, and A.A. Zyuzin, *Phys. Rev. B*, **95**, No. 15: 155124 (2017); https://doi.org/10.1103/PhysRevB.95.155124

27. A.A. Varlamov, Y.M. Galperin, S.G. Sharapov, and Y. Yerin, *Low Temp. Phys.*, **47**: No. 8 (2021); https://arxiv.org/abs/2103.04642
28. A.J. Leggett, *Progr. Theor. Phys.*, **36**, No. 5: 901 (1966); https://doi.org/10.1143/PTP.36.901
29. Y. Tanaka, *Supercond. Sci. Technol.*, **28**, No. 3: 034002 (2015); https://doi.org/10.1088/0953-2048/28/3/034002
30. D.F. Agterberg, P.M.R. Brydon, and C. Timm, *Phys. Rev. Lett.*, **118**, No. 12: 127001 (2017); https://doi.org/10.1103/PhysRevLett.118.127001
31. H. Suhl, B.T. Matthias, and L.R. Walker, *Phys. Rev. Lett.*, **3**, No. 12: 552 (1959); https://doi.org/10.1103/PhysRevLett.3.552
32. X.X. Xi, *Rep. Prog. Phys.*, **71**, No. 11: 116501 (2008); https://doi.org/10.1088/0034-4885/71/11/116501
33. H. Hosono, A. Yamamoto, H. Hiramatsu, and Y. Ma, *Mater. Today*, **21**, No. 3: 278 (2018); https://doi.org/10.1016/j.mattod.2017.09.006
34. V.B. Zabolotnyy, D.S. Inosov, D.V. Evtushinsky, A. Koitzsch, A.A. Kordyuk, G.L. Sun, J.T. Park, D. Haug, V. Hinkov, A.V. Boris, C.T. Lin, M. Knupfer, A.N. Yaresko, B. Büchner, A. Varykhalov, R. Follath, and S.V. Borisenko, *Nature*, **457**: 569 (2009); https://doi.org/10.1038/nature07714
35. A.A. Kordyuk, *Low Temp. Phys.*, **38**: 888 (2012); https://doi.org/10.1063/1.4752092
36. A.A. Kordyuk, *Low Temp. Phys.*, **44**: 477 (2018); https://doi.org/10.1063/1.5037550
37. A. Bianconi, *Natute Phys.*, **9**: 536 (2013); https://doi.org/10.1038/nphys2738
38. M. Zehetmayer, *Supercond. Sci. Technol.*, **26**, No. 4: 043001 (2013); https://doi.org/10.1088/0953-2048/26/4/043001
39. G.R. Stewart and A.L. Giorgi, *Solid State Commun.*, **28**, No. 12: 969 (1978); https://doi.org/10.1016/0038-1098(78)90650-6
40. M.S. Kim, J.A. Skinta, T.R. Lemberger, W.N. Kang, H.-J. Kim, E.-N. Choi, and S.-I. Lee, *Phys. Rev. B*, **66**, No. 6: 064511 (2002); https://doi.org/10.1103/PhysRevB.66.064511
41. N. Agrait, A.L. Yeyati, and J.M. van Ruitenbeek, *Phys. Rep.*, **377**, Nos. 2–3: 81 (2003); https://doi.org/10.1016/S0370-1573(02)00633-6
42. M. Aono and T. Hasegawa, *Proc. IEEE*, **98**, No. 12: 2228 (2010); https://doi.org/10.1109/JPROC.2010.2061830
43. G.E. Blonder, M. Tinkham, and T.M. Klapwijk, *Phys. Rev. B*, **25**. No. 7: 4515 (1982); https://doi.org/10.1103/PhysRevB.25.4515
44. S. Volkov, M. Gregor, T. Plecenik, E. Zhitlukhina, M. Belogolovskii, and A. Plecenik, *Appl. Nanosci.*, 22 February (2021); https://doi.org/10.1007/s13204-021-01734-6
45. E. Zhitlukhina, I. Devyatov, O. Egorov, M. Belogolovskii, and P. Seidel, *Nanoscale Res. Lett.*, **11**: 58 (2016); https://doi.org/10.1186/s11671-016-1285-0
46. D. Daghero and R.S. Gonnelli, *Supercond. Sci. Technol.*, **23**, No. 4: 043001 (2010); https://doi.org/10.1088/0953-2048/23/4/043001

47. V. Tarenkov, A. Shapovalov, O. Boliasova, M. Belogolovskii, and A. Kordyuk, *Low Temp. Phys.*, **47**, No. 2: 101 (2021); https://doi.org/10.1063/10.0003168
48. V. Tarenkov, A. Dyachenko, V. Krivoruchko, A. Shapovalov, and M. Belogolovskii, *J. Supercond. Nov. Magn.*, **33**: 569 (2020); https://doi.org/10.1007/s10948-019-05297-0
49. J. Talvacchio, M.A. Janocko, and J. Greggi, *J. Low Temp. Phys.*, **64**: 395 (1986); https://doi.org/10.1007/BF00681709
50. Ya.M. Blanter and M. Buttiker, *Phys. Rep.*, **336**, Nos. 1–2: 1 (2000); https://doi.org/10.1016/S0370-1573(99)00123-4
51. D. Wu, B. Dolgin, G. Jung, V. Markovich, Y. Yuzhelevski, M. Belogolovskii, and Ya.M. Mukovskii, *Appl. Phys. Lett.*, **90**: 242110 (2007); https://doi.org/10.1063/1.2748083
52. E.S. Zhytlukhina, *Metallofiz. Noveishie Tekhnol.*, **42**, No. 9: 1197 (2020) (in Ukrainian); https://doi.org/10.15407/mfint.42.09.1197
53. T. Shang, C. Baines, L.-J. Chang, D.J. Gawryluk, E. Pomjakushina, M. Shi, M. Medarde, and T. Shiroka, *npj Quantum Mater.*, **5**: 76 (2020); https://doi.org/10.1038/s41535-020-00279-1
54. A. Carrington and F. Manzano, *Physica C*, **385**, Nos. 1–2: 205 (2003); https://doi.org/10.1016/S0921-4534(02)02319-5
55. M.A. McGuire and D.S. Parker, *Phys. Rev. B*, **93**, No. 6: 064507 (2016); https://doi.org/10.1103/PhysRevB.93.064507
56. T. Shang, W. Xie, D.J. Gawryluk, R. Khasanov, J.Z. Zhao, M. Medarde, M. Shi, H.Q. Yuan, E. Pomjakushina, and T. Shiroka, *New J. Phys.*, **22**: 093016 (2020); https://doi.org/10.1088/1367-2630/abac3b
57. E.V. Clougherty, K.H. Lothrop, and J.A. Kafalas, *Nature*, **191**: 1194 (1961); https://doi.org/10.1038/1911194a0
58. R.H. Willens, E. Buehler, and B.T. Matthias, *Phys. Rev.*, **159**, No. 2: 327 (1967); https://doi.org/10.1103/PhysRev.159.327
59. K. Kuo and G. Hägg, *Nature*, **170**: 245 (1952); https://doi.org/10.1038/170245a0
60. M. Trgala, M. Žemlička, P. Neilinger, M. Rehák, M. Leporis, Š. Gaži, J. Greguš, T. Plecenník, T. Roch, E. Dobročka, and M. Grajcar, *Appl. Surf. Sci.*, **312**: 216 (2014); https://doi.org/10.1016/j.apsusc.2014.05.200
61. M. Žemlička, M. Kopčík, P. Szaby, T. Samuely, J. Kačmarčík, P. Neilinger, M. Grajcar, and P. Samuely, *Phys. Rev. B*, **102**, No. 18: 180508(R) (2020); https://doi.org/10.1103/PhysRevB.102.180508
62. A. Huang, A.D. Smith, M. Schwinn, Q. Lu, T.-R. Chang, W. Xie, H.-T. Jeng, and G. Bian, *Phys. Rev. Mater.*, **2**, No. 5: 054205 (2018); https://doi.org/10.1103/PhysRevMaterials.2.054205
63. G. Bergmann, *Phys. Rep.*, **27**, No. 4: 159 (1976); https://doi.org/10.1016/0370-1573(76)90040-5
64. M.M. Collver and R.H. Hammond, *Phys. Rev. Lett.*, **30**, No. 3: 92 (1973); https://doi.org/10.1103/PhysRevLett.30.92
65. P. Watson, B. Bandyopadhyay, Y. Bo, D. Rathnayaka, and D.G. Naugle, *Mater. Sci. Eng.*, **99**, Nos. 1–2: 175 (1988); https://doi.org/10.1016/0025-5416(88)90316-3

66. A. Banerjee, L.J. Baker, A. Doye, M. Nord, R.M. Heath, K. Erotokritou, D. Bosworth, Z.H. Barber, I. MacLaren, and R.H. Hadfield, *Supercond. Sci. Technol.*, **30**, No. 8: 084010 (2017);
https://doi.org/10.1088/1361-6668/aa76d8
67. V.B. Verma, A.E. Lita, M.R. Vissers, F. Marsili, D.P. Pappas, R.P. Mirin, and S.W. Nam, *Appl. Phys. Lett.*, **105**, No. 2: 022602 (2014);
https://doi.org/10.1063/1.4890277
68. A.E. Lita, V.B. Verma, R.D. Horansky, J.M. Shainline, R.P. Mirin, and S. Nam, *MRS Online Proceedings Library*, **1807**: 1 (2015);
https://doi.org/10.1557/opl.2015.544
69. J. Lefebvre, M. Hilke, and Z. Altounian, *Phys. Rev. B*, **79**, No. 18: 184525 (2009);
https://doi.org/10.1103/PhysRevB.79.184525
70. M. Baggioli, C. Setty, and A. Zaccone, *Phys. Rev. B*, **101**, No. 21: 214502 (2020);
https://doi.org/10.1103/PhysRevB.101.214502
71. P.B. Allen, J.L. Feldman, J. Fabian, and F. Wooten, *Phil. Mag. B*, **79**, Nos. 11–12: 1715 (1999);
https://doi.org/10.1080/13642819908223054
72. Y.M. Beltukov, C. Fusco, D.A. Parshin, and A. Tanguy, *Phys. Rev. E*, **93**, No. 2: 023006 (2016);
https://doi.org/10.1103/PhysRevE.93.023006
73. W. Steurer and J. Dshemuchadse, *Intermetallics: Structures, Properties, and Statistics* (Oxford: Oxford University Press: 2016).
74. A.B. Altman, A.D. Tamerius, N.Z. Koocher, Y. Meng, C.J. Pickard, J.P.S. Walsh, J.M. Rondinelli, S.D. Jacobsen, and D.E. Freedman, *J. Am. Chem. Soc.*, **143**, No. 1: 214 (2021);
https://doi.org/10.1021/jacs.0c09419
75. C.J. Pickard, I. Errea, and M.I. Eremets, *Annu. Rev. Condens. Matter Phys.*, **11**: 57 (2020);
https://doi.org/10.1146/annurev-conmatphys-031218-013413
76. R.G. Pearson, *J. Am. Chem. Soc.*, **85**, No. 22: 3533 (1963);
https://doi.org/10.1021/ja00905a001

Received 26.06.2021;
in final version, 12.07.2021

А.П. Шаповалов[1,2], *М.О. Білоголовський*[2,3],
О.О. Болясова[1,4], *О.А. Кордюк*[1,2]

[1] Київський академічний університет НАН України та МОН України,
бульв. Академіка Вернадського, 36; 03142 Київ, Україна
[2] Інститут металофізики ім. Г.В. Курдюмова НАН України,
бульв. Академіка Вернадського, 36; 03142 Київ, Україна
[3] Донецький національний університет імені Василя Стуса,
вул. 600-річчя, 21; 21021 Вінниця, Україна
[4] Донецький фізико-технічний інститут ім. О.О. Галкіна НАН України,
просп. Науки, 46; 03028 Київ, Україна

ДВОКОМПОНЕНТНІ СПОЛУКИ МОЛІБДЕНУ —
ПЕРСПЕКТИВНІ МАТЕРІАЛИ ДЛЯ НОВОЇ ФІЗИКИ
НАДПРОВІДНОСТИ ТА ПРАКТИТЧНИХ ЗАСТОСУВАНЬ

У цій оглядовій статті підсумовано недавній прогрес у дослідженні низькотемпературних властивостей двокомпонентних стопів та інтерметалевих сполук на основі молібдену із зосередженням головним чином на надпровідникових характеристиках, що відображають нову фізику та можливі застосування. Наведено експериментальні дані, що підтверджують двозонну/двощілинну природу ряду надпровідних сполук. Стверджується, що двокомпонентні стопи Mo–Re із переважним внеском Ренію представляють ідеальну та рідкісну тестову систему, в якій сполуки з різними співвідношеннями Re/Mo можуть бути як центросиметричними, так і нецентросиметричними, що в останньому випадку призводить до можливого змішаного надпровідного спарювання. Продемонстровано, що дві MoC-фази, — α-MoC і γ-MoC, — є топологічно нетривіальними щодо їхніх об'ємних і поверхневих зонних структур, тоді як аморфні надпровідники MoSi і MoGe є одними з перспективних матеріалів для різних надпровідникових застосувань. Завершується огляд коротким обговоренням нових тенденцій у комп'ютерному моделюванні структури та властивостей двокомпонентних сполук з використанням як прикладу нещодавно відкритої стехіометричної сполуки $MoBi_2$, а також можливостей застосування вже відомих і ще досліджуваних надпровідників на молібденовій основі.

Ключові слова: сполуки на основі молібдену, надпровідникові властивості, двозонні/двощілинні матеріали, топологічно нетривіальні фази, надпровідникові застосування. и надпровідности та практичних застосувань